Seismic behavior of circular tunnels: Influence of the initial stress state

Qiangqiang Sun, Daniel Dias

Seismic behavior of circular tunnels: Influence of the initial stress state

Qiangqiang Sun[a], Daniel Dias[b,a,c]

[a] Grenoble Alpes University, Laboratory 3SR, CNRS UMR 5521, Grenoble, France

[b] Hefei University of Technology, School of Automotive and Transportation Engineering, Hefei, China

[c] Antea Group, Antony, France

Corresponding author:
Daniel Dias, E-mail address: daniel.dias@3sr-grenoble.fr

Abstract: Tunnel construction leads to significant perturbations of the initial stress state in the surrounding soils. This implies that during a given earthquake, the seismic behavior of tunnels is probably modified. The aim of this study is to provide an estimation of the influence of the initial stress state caused by construction on the tunnel seismic response, based on the dynamic nonlinear time-history numerical analysis. The tunnel construction is simulated using the convergence-confinement method with various stress release coefficients (λ). The numerical models consider the soil-tunnel interface conditions, as well as the uncertainties in modulus degradation curves and damping ratios of soil. The frequency characteristics and intensities of input ground motions are involved as well. The results highlight that the stress release process has a more pronounced effect on the seismic axial force increments rather than the seismic bending moment increments with the effect becomes progressively larger as the input motion intensities and the stress release coefficients increase.

Keywords: Tunnel; Dynamic time-history analysis; Convergence-confinement method; Initial stress state; Soil-tunnel interaction

1. Introduction

The excavation of tunnels leads to significant perturbations of the initial stress state in the surrounding soils and thus affects the internal forces and deformations of the tunnel lining. In the last decades, growing attention has been paid to assess the stability of tunnels in various construction methods and consequences during tunneling [8-10].

On the other hand, the seismic tunnel behavior is also of great importance due to severe damages of tunnels were found in past earthquakes [23,24,30,33,36,43,44,46]. Despite many important influencing factors have been recently identified [16,40], the influence of the stress redistribution caused by tunnel excavation on the earthquake damage is seldom evaluated due to lack of construction information. Indeed, the stress release process is not easy to be precisely quantified during tunneling or in the experimental test.

Recently, a series of centrifuge tests were performed to study the tunnel seismic behavior and to validate the accuracy of various soil constitutive models [1,5,15,17,28,29,42]. The numerical simulations highlighted that more sophisticated constitutive models were not always performing better than simplified ones, mainly due to the uncertainties which exist in the developed numerical models (i.e., soil-tunnel interface, parameter calibration, damping) [3]. The tunnel construction process has been involved in some numerical studies, but the influence of the stress release process on the seismic tunnel behavior was not fully evaluated [6,25,31]. Corigliano et al. [6] analyzed the seismic response of the Serro Montefalco tunnel (Italy) using the nonlinear pseudo-static approach. In their study, a stress release coefficient of 0.75 was adopted to simulate the construction stages of the tunnel prior to the earthquake loading. Kontoe et al. [25] compared numerical results with analytical solutions using finite element method with a stress release coefficient of 0.5. Ma et al. [31] performed a numerical analysis to investigate the role of the burial depth on the seismic behavior of subway station accounts for the ground loss ($\zeta = 0.5$ %) induced by construction.

Gomes [14] provided the first study of construction-induced stress disturbance effect on the seismic behavior of tunnels, to the authors' knowledge, that considered the soil nonlinearity using an advanced multi-mechanism elastoplastic model. Nevertheless, Gomes [14] did not consider the slippage and separation at the soil-tunnel interface. More recently, Sun and Dias [39] investigated the stress release during tunneling on seismic tunnel behavior by the pseudo-static method accounted for the influence of Young's modulus of soil, the coefficient of earth pressure at rest, the applied shear strain and the

constitutive model of soil. It was worth noting that the dynamic soil behavior, the inertia force of the tunnel and the dynamic amplification of the soil could not be considered in the pseudo-static analysis. These effects are probably significant for evaluating the construction-induced stress redistribution on the seismic behavior of tunnels, which can only be captured by dynamic nonlinear time-history analysis.

This paper aims to evaluate how the initial stress state caused by construction affects the seismic behavior of tunnels by using a series of dynamic nonlinear time-history numerical analyses in two-dimensional. The Bologna-Florence high-speed railway line tunnel project in Italy is adopted as the reference case. Prior to the earthquake analysis, the tunnel excavation is simulated using the convergence-confinement method to obtain various initial stress states in the surrounding soils and the corresponding static lining forces and deformations. Then, six earthquake loadings are applied to evaluate the effect of the initial stress states on the tunnel seismic response accounting for the input motion intensities and frequency characteristics. The numerical model assumes both the no-slip and full-slip conditions between the soil and the lining, which is consistent with the commonly used assumption of the analytical solutions. Based on the numerical predictions, the relationships between the stress release coefficients and the normalized lining force increments in a wide range of cases are presented. Finally, the possible influences of the stress redistribution caused by construction on the surface ground motion, as well as the uncertainties in modulus reduction curves and damping ratios in numerical models are discussed.

2. Convergence-confinement method

Only a three-dimensional model can accurately simulate the tunnel excavation due to the tunnel advancement which induces a stress redistribution and three-dimensional deformation. However, due to the complexity and the time-consuming of this type of model, the tunneling process is often modeled using two-dimensional plane strain conditions [9,21].

The convergence-confinement method (CCM) which accounts for the 3D effects by replacing the ground to be excavated by a fictitious pressure is the one that has been widely used among the available equivalent approaches. Previous works pointed out that this method works well to simulate tunnel-induced surface settlement and lining forces in two-dimensional numerical studies [7,8,34]. The radial stress, σ_r, acting on the tunnel periphery is given as follows:

$$\sigma_r = (1-\lambda)\sigma^0 \quad (1)$$

$$\lambda = \frac{U_r^{(x)}}{U_r^{\infty}} \quad (2)$$

$$U_r^{\infty} = \frac{1+\mu}{E}\sigma^0 r \quad (3)$$

where λ is the stress release coefficient; σ^0 is the initial stress in the ground medium; $U_r^{(x)}$ is the radial component of displacement at a distance x behind the face; and U_r^{∞} is the radial component of displacement at a distance behind the face considered as infinite.

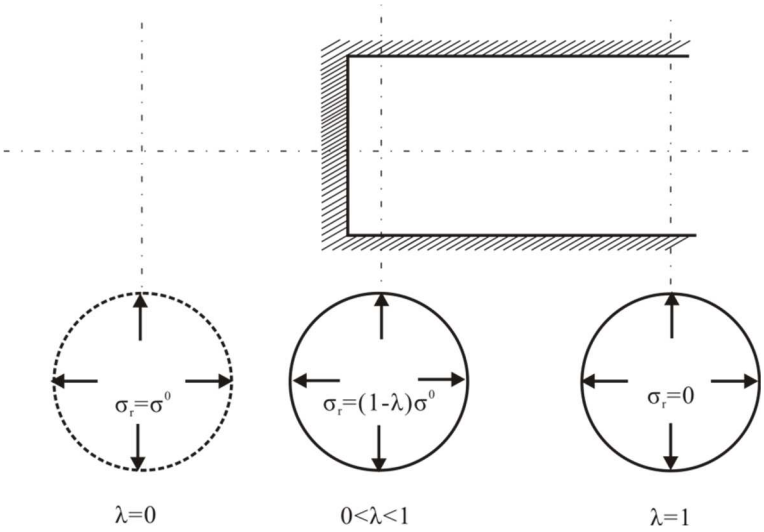

Fig. 1. Evolution of tunnel convergence with face advance

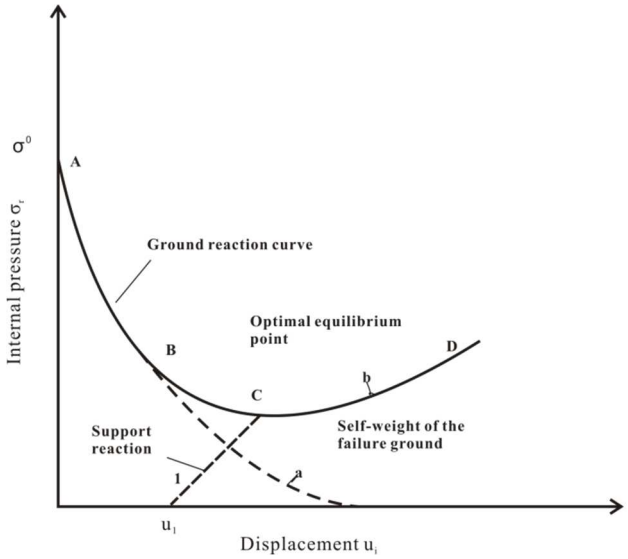

Fig. 2. CCM: 1 support reaction line u_1 and tunnel boundary displacements before the installation of the lining

The two-dimensional tunneling problem is illustrated in Fig. 1. The tunneling process is represented

by increasing the λ value from 0 to 1. Fig. 2 shows the main characteristics of the convergence-confinement method. The convergence curve corresponds to the internal pressure versus the tunnel radial displacement. The radial displacement of the tunnel increases as the internal pressure decreases. The tunnel can be self-stabilized without a liner (curve (a) in Fig. 2) or the surrounding ground can fail which leads to an increase in the ground load acting on the tunnel lining (curve b in Fig. 2). In the latter case, a liner must be installed to keep the stability of the tunnel [9].

3. Two-dimensional numerical modeling

3.1 Model parameters

In this study, the Bologna-Florence high-speed railway tunnel project in Italy is adopted as the reference case. This project is part of the Italian high-speed railway network. The external excavation diameter of the tunnel equals to 9.4 m and the internal diameter equals to 8.3 m. The tunnel section equals to 46 m^2. The lining forces and stability of the tunnel during the construction stages have been analyzed in the previous studies [7,9].

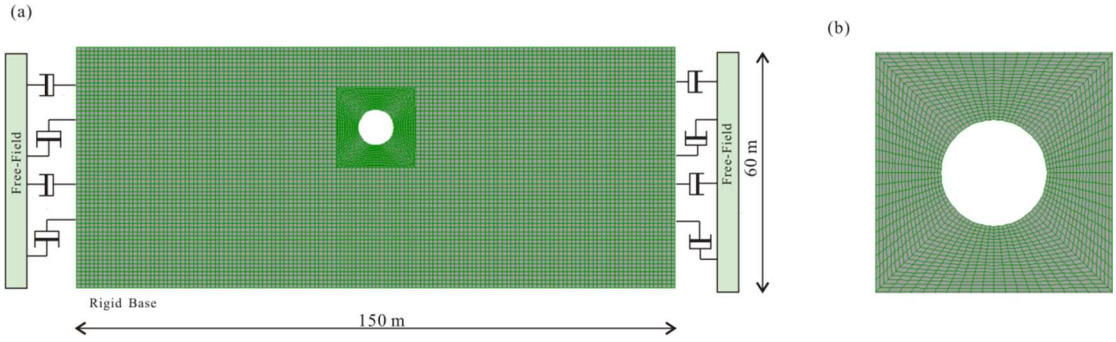

Fig. 3. Soil-tunnel numerical model: (a) meshes and boundary conditions; (b) refined meshes around the tunnel

Fig. 3 shows the two-dimensional numerical model using the FLAC finite difference element code [20]. The model has a height of 60 m and a width of 150 m. It is assumed that the behavior of the tunnel lining is linear-elastic and the behavior of the surrounding soil is simulated with an elastic-perfectly plastic constitutive model (Mohr-Coulomb (MC) failure criterion [7,9]). This criterion is frequently used in the nonlinear seismic analyses of tunnels [4,38] despite its simplicity. Parameters of the tunnel support and of the soil adopted in this study are given in Table 1 [7,9].

Table 1. Parameters of the tunnel

Parameters	Symbol	Value	Unit
Properties of clayed sand			
Unit weight	γ_m	17	kN/m^3
Initial Young's modulus	E_m	150	MPa
Poisson's ratio	μ_m	0.3	-
Internal friction angle	φ	37	°
Dilatancy angle	ϕ	0	°
Cohesion	c	5	kPa
Lateral earth pressure factor	K_0	0.5	-
Depth	H	20	m
Properties of tunnel lining			
Young's modulus	E_l	35,000	MPa
Poisson's ratio	μ_l	0.15	-
Lining thickness	T	0.4	m
External diameter	D	9.1	m

Hysteretic damping models used in the dynamic analysis impose the shear-modulus reduction and damping ratios as a function of cyclic shear strains. A built-in hysteretic damping model [20] is selected for the dynamic analysis.

$$G_{secant} = s^2(3 - 2s) \tag{4}$$

$$s = \frac{L_2 - L}{L_2 - L_1} \tag{5}$$

where L is the logarithmic strain and L_1 and L_2 are the extreme values of logarithmic strain.

Shear modulus reduction curves under different mean effective pressures, p', or depths reported by several researchers [3,11,12] are presented in Fig. 4. It can be found that these curves are strongly dependent on the p' or depth, and different curves are probably obtained even for the same value of p' (i.e, p'=400 kPa). It should be clarified that the hysteretic damping used here is not as a primary way to simulate yielding, but as a supplement to the nonlinear constitutive model (linear elastic perfectly plastic in this study). In the absence of laboratory data, the shear modulus reduction curve suggested by Sun et al. [35] is used (dash green line). This curve is close to the data of [3] for p'=200 kPa which corresponds to the location of the tunnel springline.

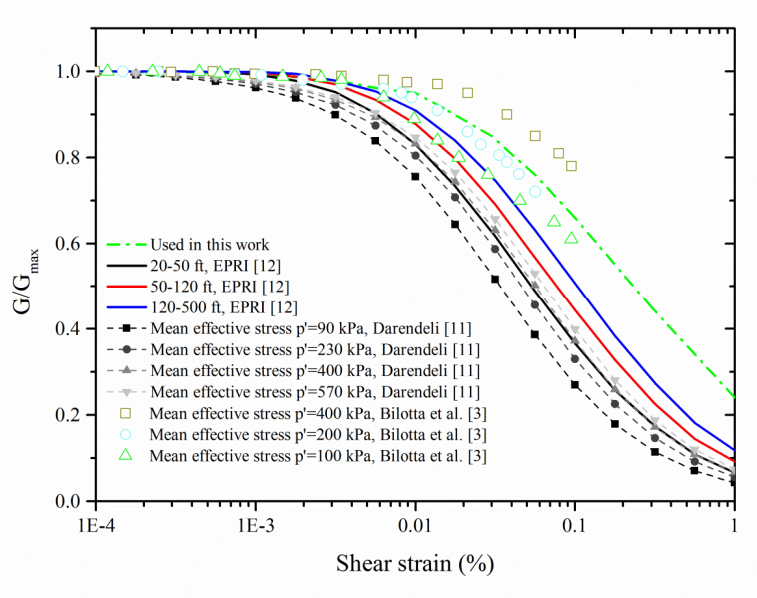

Fig. 4. Shear modulus reduction curve

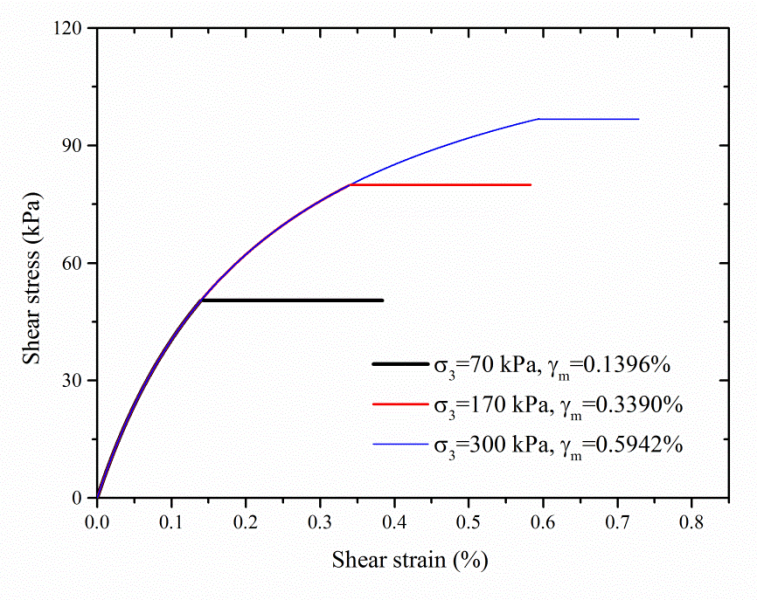

Fig. 5. Shear stress/strain curves – Linear elastic perfectly plastic (Mohr-Coulomb shear failure criteria) constitutive model with hysteretic damping under different confinement pressures

Fig. 5 presents the shear stress/strain curves under different confinement pressures (σ_3) when a hysteretic damping is combined with the linear elastic perfectly plastic MC model. The MC model has a constant elastic shear modulus and a constant yield stress. It is not able to simulate the soil shear modulus degradation in the elastic range. Hence, introducing a hysteretic damping permits to induce energy dissipation below the yield strain γ_m. Whereas, the dissipated energy (area enclosed in the shear stress/strain loop) in the plastic range, can be attributed to both the hysteretic damping and MC model

itself. Compared to the MC model only, the inclusion of hysteretic damping increases the overall damping ratio during the dynamic analysis [20], which monotonically increases with the shear strain amplitude.

The soil-tunnel interfaces are modeled as a linear spring-slider system following the Mohr-Coulomb shear failure criterion. The relative movement and separation are controlled by the normal stiffness K_n and the shear stiffness K_s. The apparent stiffness of a zone in the normal direction is:

$$\max\left[\frac{K+\frac{4}{3}G}{\Delta Z_{min}}\right] \quad (6)$$

where K and G are the bulk and shear modulus respectively, and ΔZ_{min} is the smallest width of the adjoining zone in the normal direction. According to the Users' manual [20], nearly ten times the equivalent stiffness of the stiffest neighboring zone is generally used to calculate the normal stiffness. By the sensitivity analysis, $K_n = 4 \times 10^9\ N/m^3$ is adopted here. Too larger normal stiffness value is not recommended because of expensive computational cost. The shear stiffness depends on the degree of the slippage, and a very high stiffness value prevents movement on the interface. Through checking the soil-tunnel interface states in the sensitivity analysis (see Fig. 8), the shear stiffness of $4 \times 10^9\ N/m^3$ can properly present the no-slip condition. For the full-slip case, a nominal value of the shear stiffness ($K_s = 1 \times 10^3\ N/m^3$) is used as recommended in Kontoe et al. [25].

The boundaries conditions used in the numerical models are as follows: the nodes along the lateral boundaries are fixed in the horizontal direction; meanwhile, both the horizontal and the vertical directions are fixed at the base of the model in the static analysis. For the dynamic analysis, the side boundaries use the free-field boundary conditions and the vertical velocity along the model bottom is fixed to simulate a rigid base condition.

In dynamic simulations, the frequency-dependent viscous damping is generally introduced by means of the Rayleigh formulation. Owing to the inherent limitation of the Rayleigh damping, the numerical results can be significantly affected by the Rayleigh damping determination method [27,32,38]. According to the recommendation of Kwok et al. [27], the fundamental site frequency and five times the fundamental site frequency are selected to determine the center frequency corresponding to a $f_{min} = 1.8$ Hz in this study. With regard to the minimum damping ratio ζ_{min}, a ratio of 3.0 % is determined. The influence of the minimum damping ratio on the numerical predictions will be presented later.

Six real ground motions (Table 2) with diverse frequency components are used as the seismic input motions in order to capture the influence of the frequency characteristics on the tunnel seismic behavior, as

plotted in Fig. 6. In order to reduce the computational cost, the ground motion duration time is set to 25 s, which contains the peak acceleration and critical frequency characteristics of the original ground motions. All the input ground motions are scaled to three amplitudes (0.1 g, 0.2 g, and 0.4 g) to account for the effect of the input motion intensities. A low-pass filter is applied to remove the frequencies higher than 15 Hz in order to ensure the numerical stability and the accuracy of the wave propagation within the model. The acceleration time histories are applied along the model bottom to simulate the vertically propagating ground motions. Based on the well-known equation of Kuhlemeyer and Lysmer [26], the maximum mesh size used here is equal to 1 m and the meshes around the tunnel are refined, as illustrated in Fig. 3b.

Table 2. Input ground motions

Number	Earthquake event	Station name	PGA (g)	Predominant frequency (Hz)
GM1	Imperial Valley	USGS station 5115	0.3152	7.1
GM2	Friuli	Tomezzo (000)	0.3513	3.9
GM3	Hollister	USGS station 1028	0.1948	2.5
GM4	Kobe	Kakogawa (cue90)	0.3447	6.3
GM5	Loma Prieta	090CDMG station 47381	0.3674	4.5
GM6	Northridge	090CDMG station 24278	0.5683	3.8

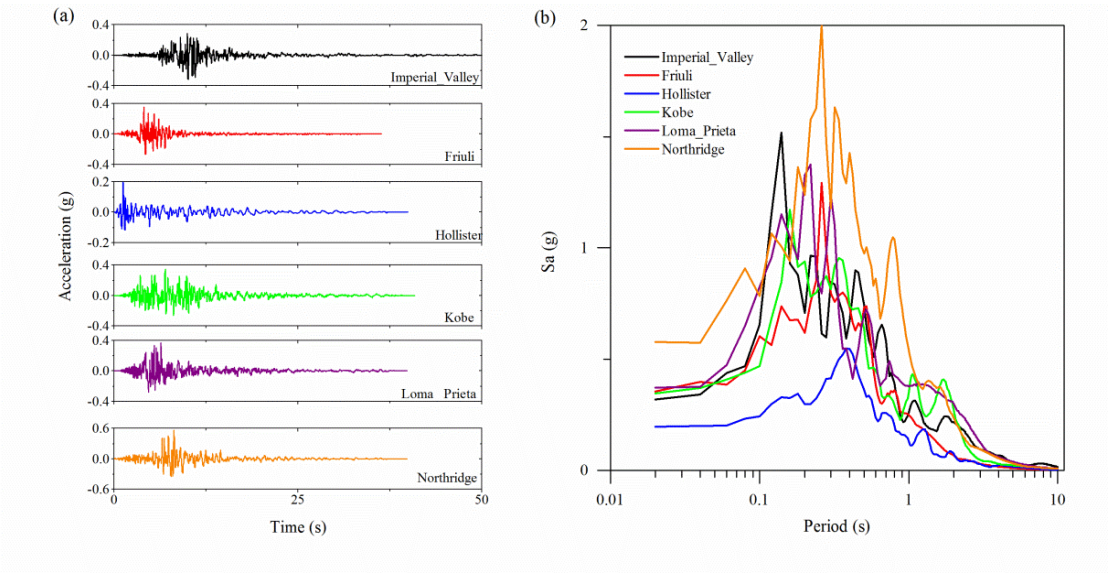

Fig. 6. Input ground motions (a) Acceleration time histories (b) Fourier amplitude spectra

3.2 Stress release phase

The tunneling induced stress release process is simulated using the convergence-confinement method through the following steps:

(a) Generation of the initial geostatic stress under the gravity loads and the lateral earth pressure.

(b) The full tunnel face is excavated and a radial pressure is simultaneously applied to the tunnel boundaries. The radial pressure is then reduced step by step until it reaches the specified stress release coefficient λ and achieve a new equilibrium state.

(c) Installation of the tunnel lining then completely releases the residual radial pressure.

In practice, the stress release coefficients are usually specified according to back analysis of experimental or field monitoring data obtained during the tunneling process [19,22]. In the present study, four stress release coefficients of 0, 0.35, 0.5, and 0.7 are adopted. The value $\lambda = 0$ means that the tunneling process is not taken into account, which is frequently used in most of numerical analyses and analytical solutions. In this study, the complete stress release process ($\lambda = 1.0$) is not adopted due to the fact that the calculation cannot reach an equilibrium state (large deformation of soil occurs), which is also not realistic for shallow tunnels constructed in soft soil.

4. Numerical results

4.1 Static analysis

Before the dynamic analyses, the static analyses are performed first to determine the initial stress states in the surrounding soils and the static lining forces and deformations. Fig. 7 shows the distribution of the static lining forces with different stress release coefficients for the two soil-tunnel interface conditions at the end of the static analysis.

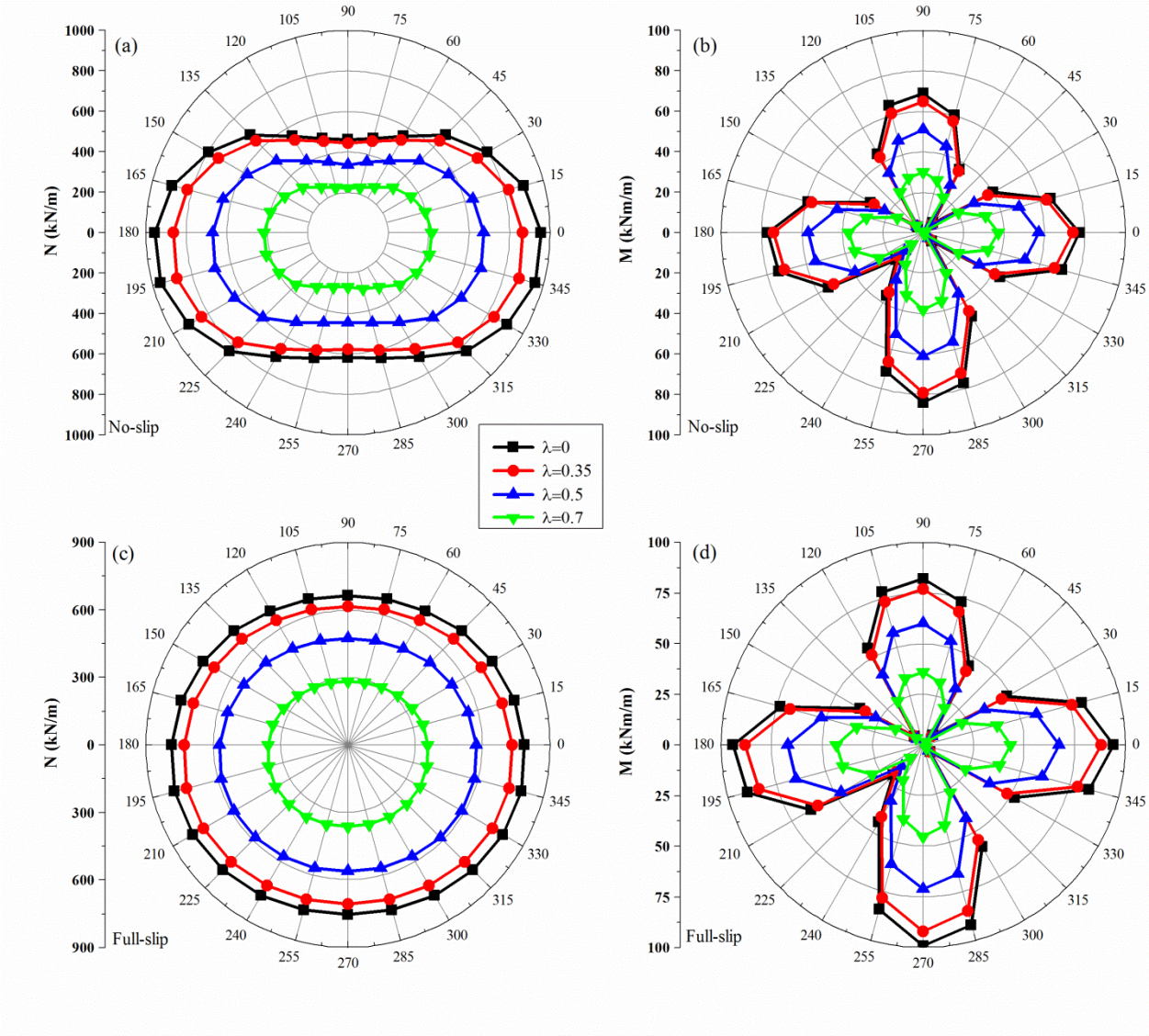

Fig. 7. Lining forces after the lining installed: (a) axial forces, no-slip; (b) bending moments, no-slip; (c) axial forces, full-slip; (d) bending moments, full-slip

As can be seen, an increase in the stress release coefficient generally results in a reduction in the lining forces. In addition, the distributions of bending moment are similar for both the no-slip and full-slip cases. For the no-slip case, the maximum axial forces appeared at the two tunnel sides (Fig. 7a) due to the low value of the lateral earth pressure coefficient at rest ($K_0 = 0.5$); while for the full-slip case the axial forces seem to be almost constant in the lining. This can be contributed to the slippage and separation occurred between the soil and the tunnel due to the very small shear stiffness in the full-slip condition [37]. Fig. 8 shows the maximum shear stress in the surrounding soil and the interface. It can be seen that the maximum interface shear stress (126 kPa) is larger than the maximum soil shear stress (95 kPa) for the no-slip condition, preventing the occurrence of the slippage at the soil-tunnel interface. However, the

maximum interface shear stress is significantly smaller (2.1 Pa) than the one in the surrounding soil (130 kPa) for the full-slip condition, providing a negligible shear resistance to the slippage. It illustrates that the interface parameters selected in this study are appropriate to respectively simulate the no-slip and full-slip conditions.

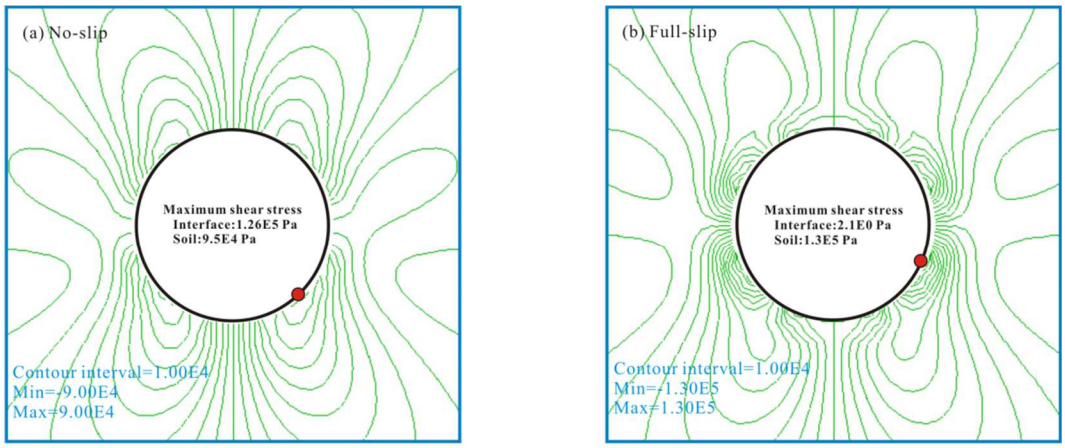

Notes: red point presents the location of the soil maximum shear stress

Fig. 8. Maximum soil shear stress without considering stress relief: (a) no-slip; (b) full-slip

To further validate the accuracy of the soil-tunnel interface parameters, Table 3 presents the comparison of the calculated maximum axial forces and bending moments by the numerical analysis and two analytical solutions [2,13] for the no-slip condition without considering stress release. The equations employed by the two analytical solutions are summarized in the Appendix. Both the analytical solutions over-estimate the lining forces, particularly for the axial forces calculated by the Erdmann [13] solution (+43%). In general, analytical solutions assume a uniform stress field for a deep tunnel in an elastic soil. However, the tunnel in this study cannot be considered as a deep tunnel and the stress at the tunnel crown ($\sigma_v = 258$ kPa) is smaller than the one at the tunnel invert ($\sigma_v = 408$ kPa). It thus leads to a non-uniform stress field. Furthermore, the nonlinearity soil behaviour affects the lining forces in the numerical predictions, as stated in [45].

Table. 3. Comparison of the calculated axial forces and bending moments by numerical analysis and analytical solutions for the no-slip condition and for λ=0

	Numerical analysis	Bakker [2]	Erdmann [13]
Axial force, N (kN/m)	959	1233 (+26%)	1374 (+43%)
Bending moment, M (kNm/m)	84	86 (+2%)	117 (+39%)

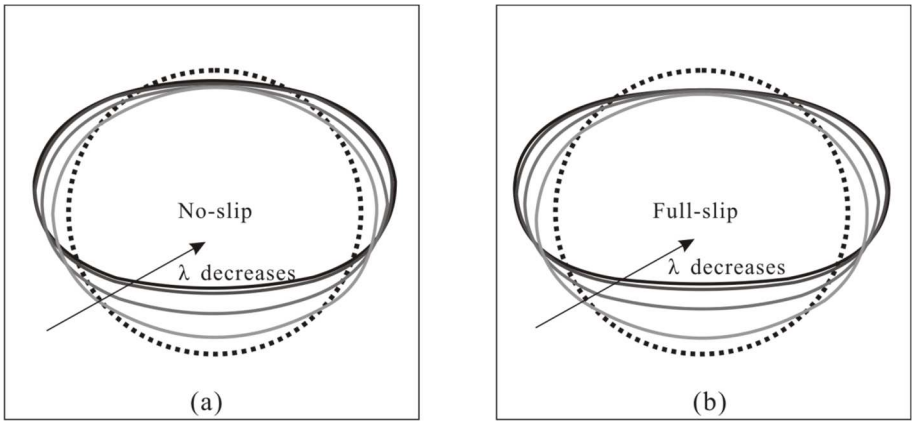

Fig. 9. Tunnel lining deformations for different stress release coefficients: (a) no-slip; (b) full-slip (Magnification factor: 300)

Fig. 9 compares the tunnel deformations for different stress release coefficients, showing that the tunnel lining deforms less when a larger stress release coefficient is employed, both in terms of horizontal and vertical deformations (Table 4). The stress release process reduces the stress acting on the tunnel lining which then produces less deformation, as expected. Table 4 also depicts that the deformation is more significant for the full-slip condition.

Table. 4. Horizontal and vertical deformations of tunnel lining for different stress release coefficients

	Horizontal deformation (cm)		Vertical deformation (cm)	
λ	No-slip	Full-slip	No-slip	Full-slip
0	0.52	0.63	0.62	0.73
0.35	0.49	0.59	0.58	0.68
0.5	0.38	0.46	0.45	0.53
0.7	0.24	0.29	0.28	0.33

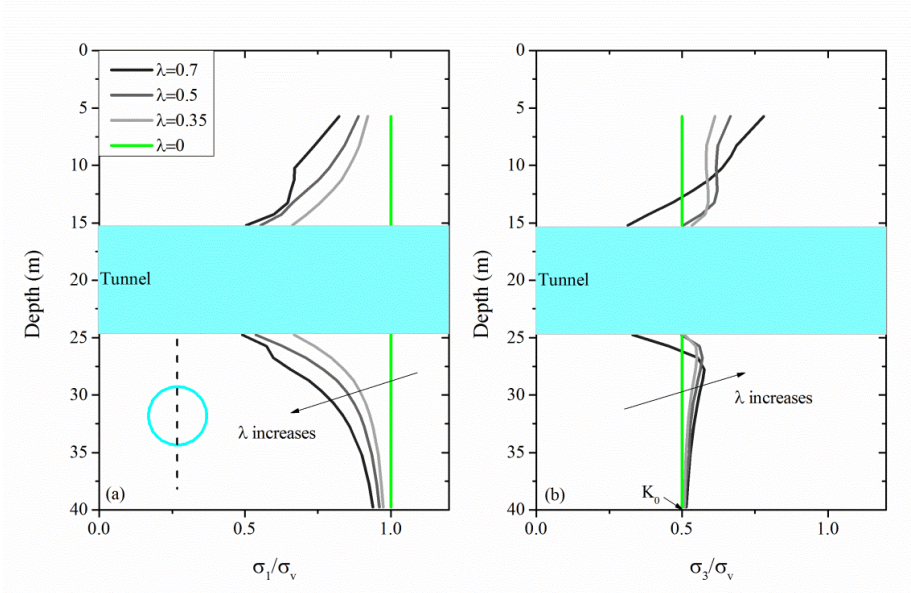

Fig. 10. Normalized vertical and horizontal stress around the tunnel

The mobilization of the earth pressure around the tunnel for different stress release coefficients is presented in Fig. 10, in terms of the normalized vertical (σ_1/σ_v) and horizontal stress (σ_3/σ_v) calculated along the tunnel centerline. Both the values of σ_1/σ_v and σ_3/σ_v decrease around the tunnel due to the stress release process, particularly for the higher stress release coefficients. In addition, larger lateral earth pressure coefficients (σ_3/σ_v) are predicted for higher λ at some positions, due to the soils are in a passive state when move towards the tunnel.

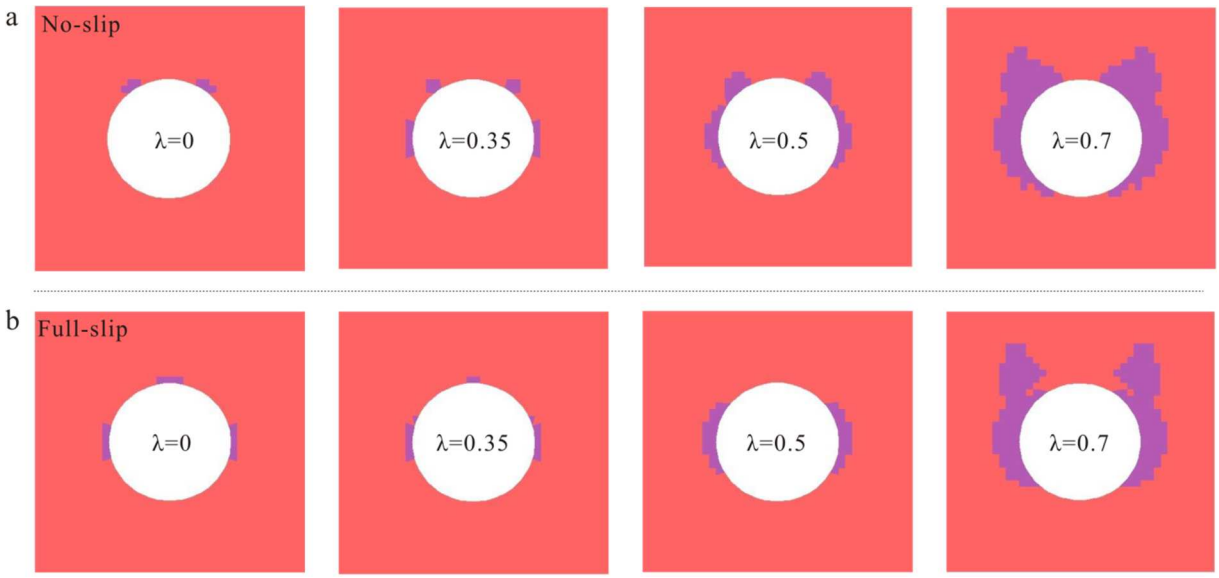

Fig. 11. Plastic zones after the lining installation versus the stress release coefficients: (a) no-slip case; (b) full-slip case

Fig. 11 presents the plastic zones in the surrounding soil versus four stress release coefficients for the no-slip and full-slip cases. As can be clearly seen, the plastic zone becomes larger as the stress release coefficient increases, particularly for the tunnel sides and shoulders. It is attributed to the displacement of soil around the tunnel boundary becomes progressively larger as the stress release coefficient increases (Fig. 2). When $\lambda < 0.35$, most of the surrounding soil elements do not reach the plastic state and, stay in an elastic state. It seems that no-slip case induces a slightly larger plastic zone than full-slip case. However, as compared to the stress release process, the effect of soil-tunnel interface conditions on the plastic zone seems unimportant.

4.2 Dynamic analysis

After the tunnel construction and liner installation phases, various ground motions are applied to

investigate the seismic tunnel response under different initial stress states. Fig. 12 presents the time histories of seismic-induced internal forces at the tunnel shoulder ($\theta = 45°$) for the Kobe earthquake with an amplitude of $PGA = 0.4$ g.

The axial force increases at the beginning of the earthquake due to the input motion intensity increases, especially for the higher stress release coefficient ($\lambda = 0.7$). At the end of the earthquake, a significant residual axial force is left on the lining due to the irreversible plasticity deformations of soil [4,24,41]. This is more evident when larger stress release coefficient is employed. However, the stress release process has a minor influence on the bending moment time histories, and no clear trend is found, as shown in Figs. 12b and d.

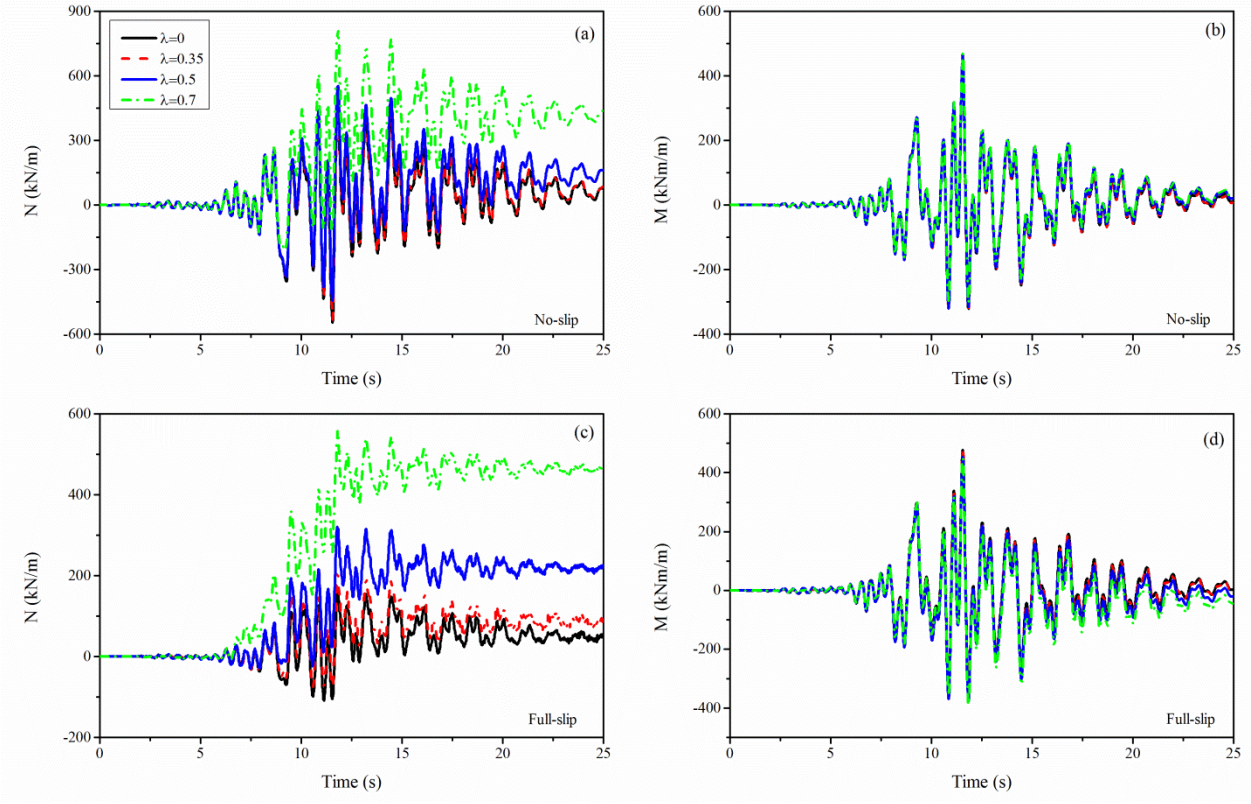

Fig. 12. Time histories of the seismic internal force increments: (a) axial force, no-slip; (b) bending moment, no-slip; (c) axial force, full-slip; (d) bending moment, full-slip

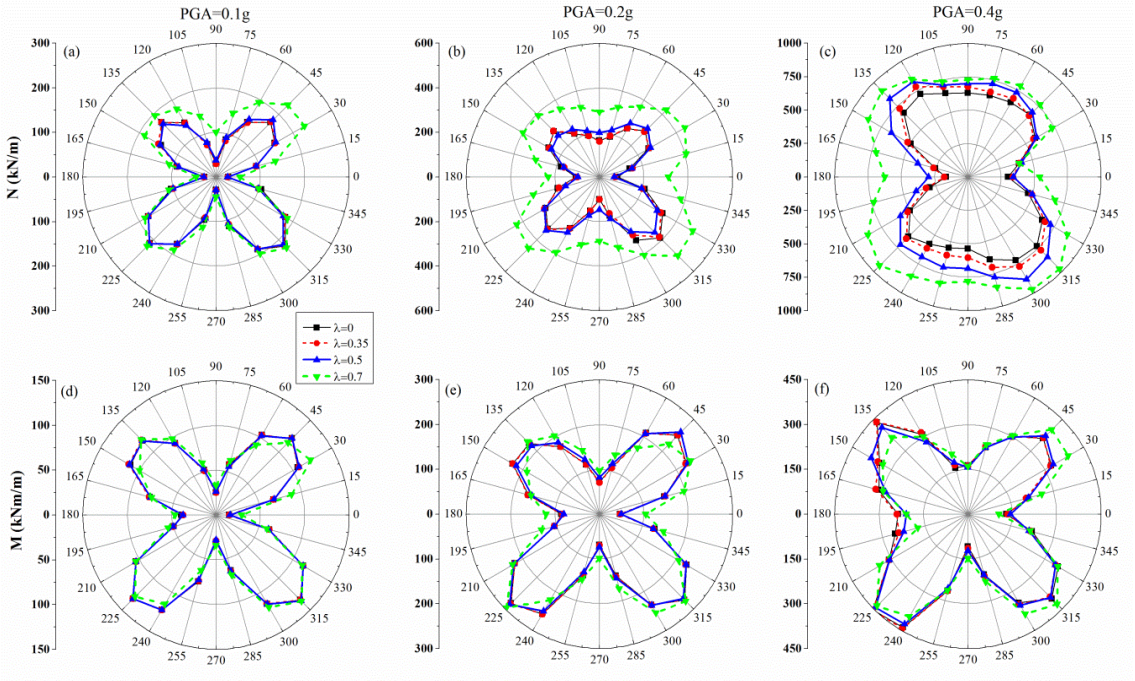

Fig. 13. Distribution of the maximum absolute seismic internal force increments: (a)~(c) axial force; (d)~(f) bending moment (No-slip case)

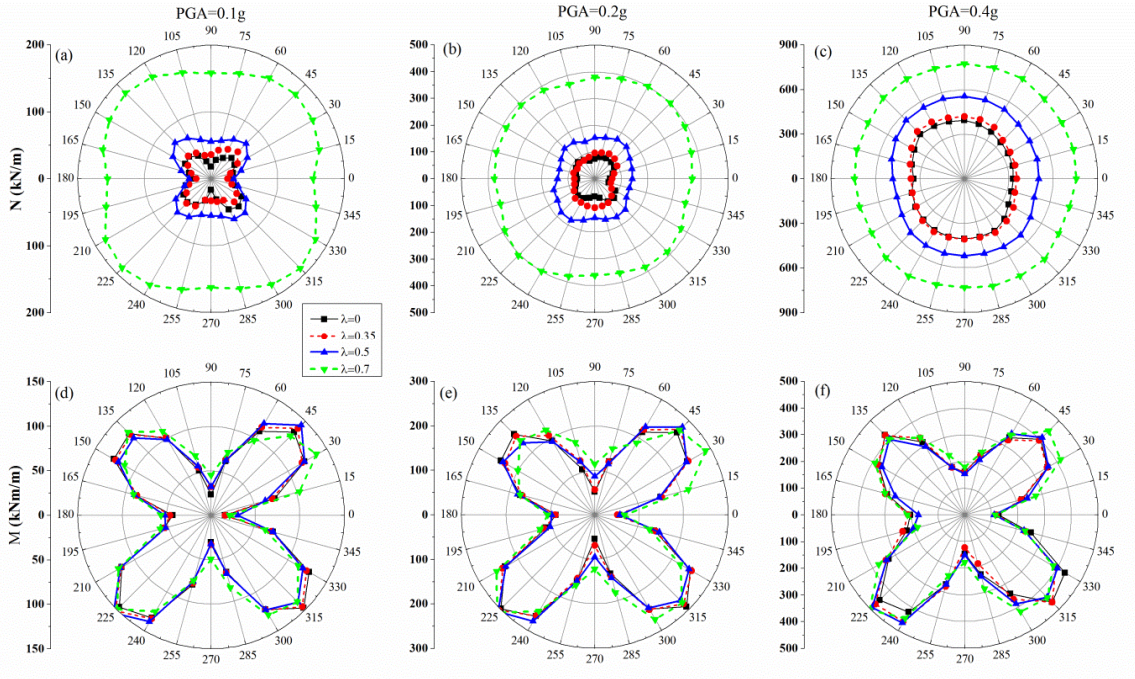

Fig. 14. Distribution of the maximum absolute seismic internal force increments: (a)~(c) axial force; (d)~(f) bending moment (Full-slip case)

Figs. 13 and 14 compare the distributions of the maximum absolute internal force increments induced by the Kobe earthquake under various λ values and PGAs for the no-slip and full-slip cases, respectively. All the analyses illustrate that a noticeable seismic internal force increment appears near the shoulder and

the arch for the no-slip case and the bending moment for the full-slip case. However, similar to the static analysis results, the seismic axial force increments are relatively uniform along the tunnel circumference for the full-slip case. Sedarat et al. [37] studied the effect of soil-tunnel contact condition on the response of tunnels based on a Coulomb friction law. They stated that the axial force almost stays constant in the case of tunnel ovaling without friction ($f = 0$ in their studies corresponds to the full-slip case here). Higher stress release coefficient leads to a larger seismic axial force increment, while the bending moments are slightly influenced by the stress release process. This is in agreement with the findings of Gomes [14] and quasi-static analyses of Sun and Dias [39].

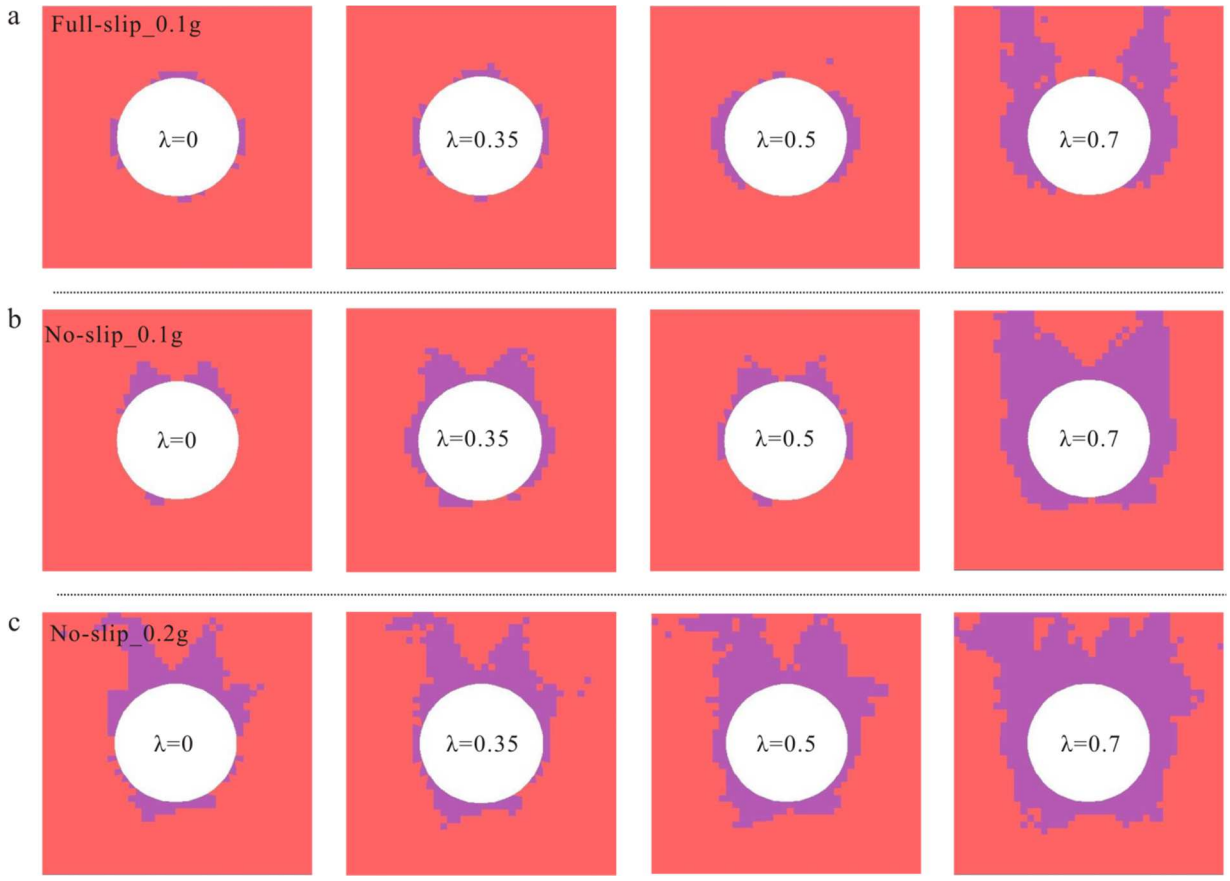

Fig. 15. Plastic zones around the tunnel at the end of the Kobe earthquake versus stress release coefficients: (a) full-slip, 0.1g; (b) no-slip, 0.1g; (c) no-slip, 0.2g

Fig. 15 shows the typical plastic zones in the surrounding soil at the end of the Kobe earthquake. The plastic zone is becoming progressively larger as the stress release coefficients and the input motion intensities increase, as expected. Consistent with the static results, the no-slip case generally results in larger plastic zones as compared to the full-slip case. This could be attributed to the tangential forces around the lining boundary are larger due to no relative movement is allowed (Fig. 8). Huo et al. [18] and

Tsinidis et al. [41] also reported that the "strong" connection between the soil and the lining increases the soil plastic strain around the flexible tunnel while the plastic strain is decreased for the full-slip condition.

In order to quantify the stress release impact on the seismic-induced internal force increments, two normalized parameters are defined as follows:

$$R_N = \frac{N_{seismic\_\lambda_i}}{N_{static\_\lambda_i}} \quad (7)$$

$$SR_N = \frac{N_{seismic\_\lambda_i}}{N_{seismic\_\lambda_0}} \quad (8)$$

where R_N is the ratio of the seismic axial force increment compared to the static one at the same stress release coefficient λ_i, SR_N is the ratio of the seismic axial force increment at the specific stress release coefficient λ_i compared to the one in the case of no stress release (λ=0). The definition of these coefficients for the bending moment is same to the ones for the axial forces.

Fig. 16 shows the R_N and R_M ratios versus the stress release coefficients for the no-slip and full-slip cases, corresponding to six ground motions and three PGAs. As can be seen, similar trends are captured by different ground motions. The much larger R_M ratios are calculated due to the relatively lower static bending moment (Fig. 7). The effect becomes progressively larger as the stress release coefficients and the input motion intensities increase, particularly for the no-slip case. The maximum R_M ratio increases up to 12 while it is around 2.5 for the R_N ratio. Similar to the static analysis results, the changes in the R_N and R_M ratios are negligible when the value of λ is smaller than 0.35, while the ratios rapidly increase when $\lambda > 0.35$. The results of the no-slip cases are in accordance with the Gomes [14] findings.

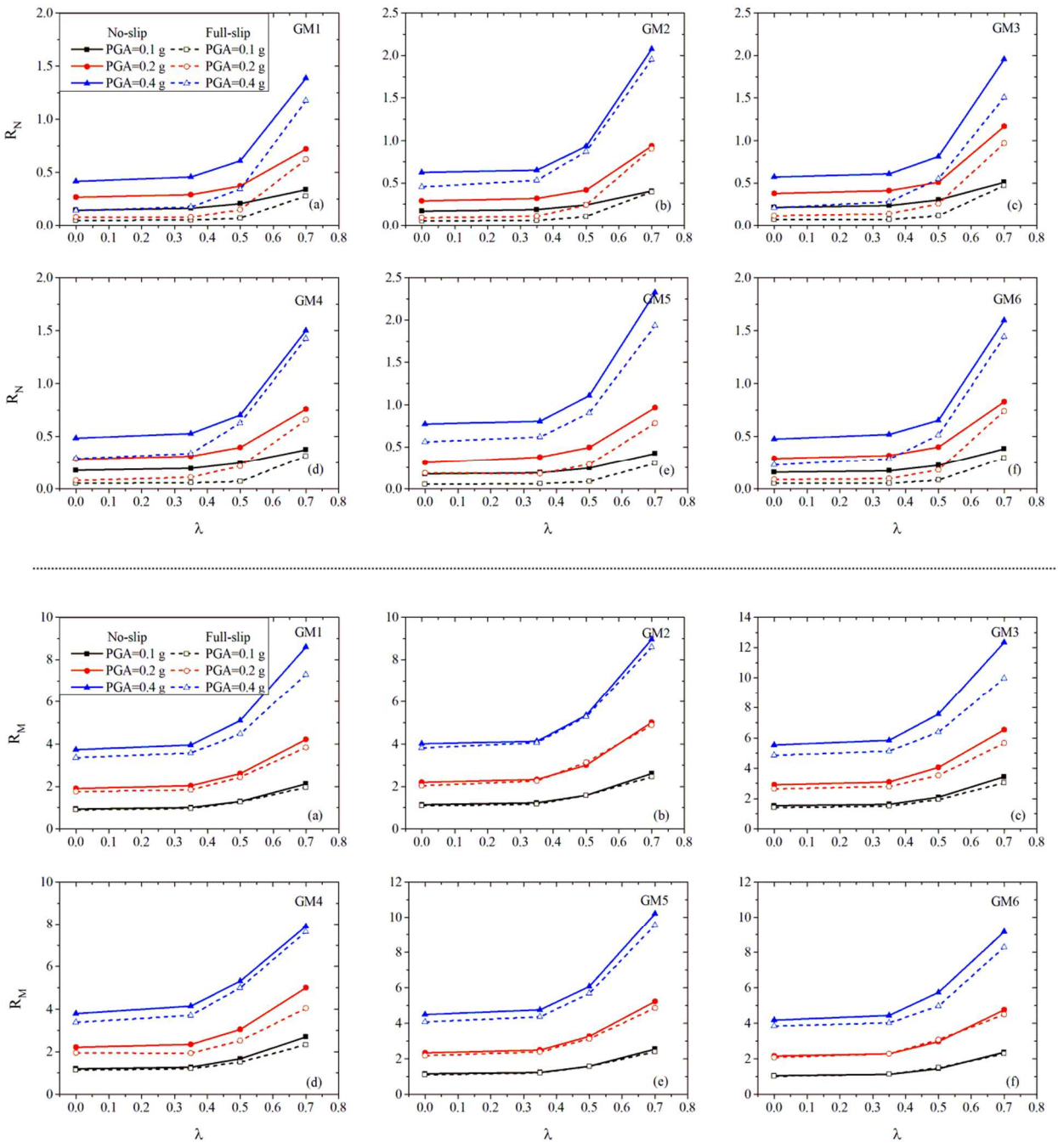

Fig. 16. R_N (upper) and R_M (lower) ratios versus the stress release coefficients for different ground motions and amplitudes

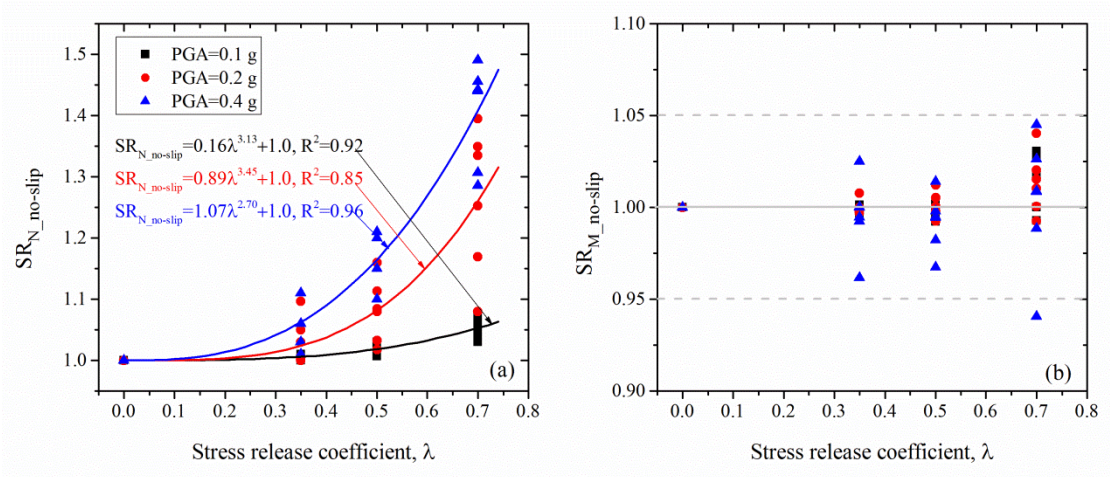

Fig. 17. Relationship between SR ratios and stress release coefficients: (a) axial forces; (b) bending moments (No-slip case)

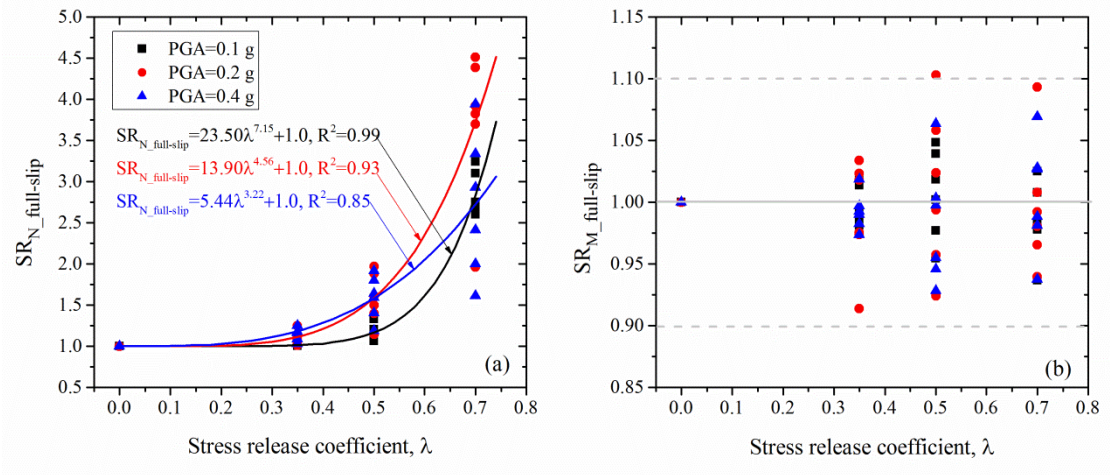

Fig. 18. Relationship between SR ratios and stress release coefficients: (a) axial forces; (b) bending moments (Full-slip case)

The ratios (e.g., SR) between the maximum seismic-induced internal force increments at a specific stress release coefficient and the ones at $\lambda = 0$ are respectively presented in Figs. 17 and 18 for the no-slip and full-slip cases. The SR_N ratio increases with increasing stress release coefficient for the two soil-tunnel interaction conditions. For the no-slip case, the ratio varies from 1.0 to 1.5, while it changes from 1.0 to 4.5 for the full-slip case. This contributes to a lower axial force increment is calculated in the case of $\lambda = 0$ for the full-slip condition (Fig. 14a~c). Concerning the bending moments, the stress release process shows a minor influence on the SR_M ratios and the trend observed is not clear. The no-slip conditions predict the SR_M ratios change from 0.95 to 1.05, while a slightly larger variation (0.9~1.1) is observed for the full-slip conditions.

Higher input motion intensity leads to larger R_N ratios, but the SR_N ratios do not always vary in the same trend. For the no-slip conditions (Fig. 17a), the SR_N ratio increases as the input motion intensity

increases. The effect is becoming progressively larger as the stress release coefficient increases. However, the full-slip conditions present the same trend only for the stress release coefficient $\lambda < 0.5$, while the maximum ratio is reported when $PGA = 0.2g$ in the case of stress release coefficient $\lambda = 0.7$ (Fig. 18a). This phenomenon can be due to the larger axial force increment caused by the earthquake in the case of $PGA = 0.4g$ when $\lambda = 0$ (Fig. 14c).

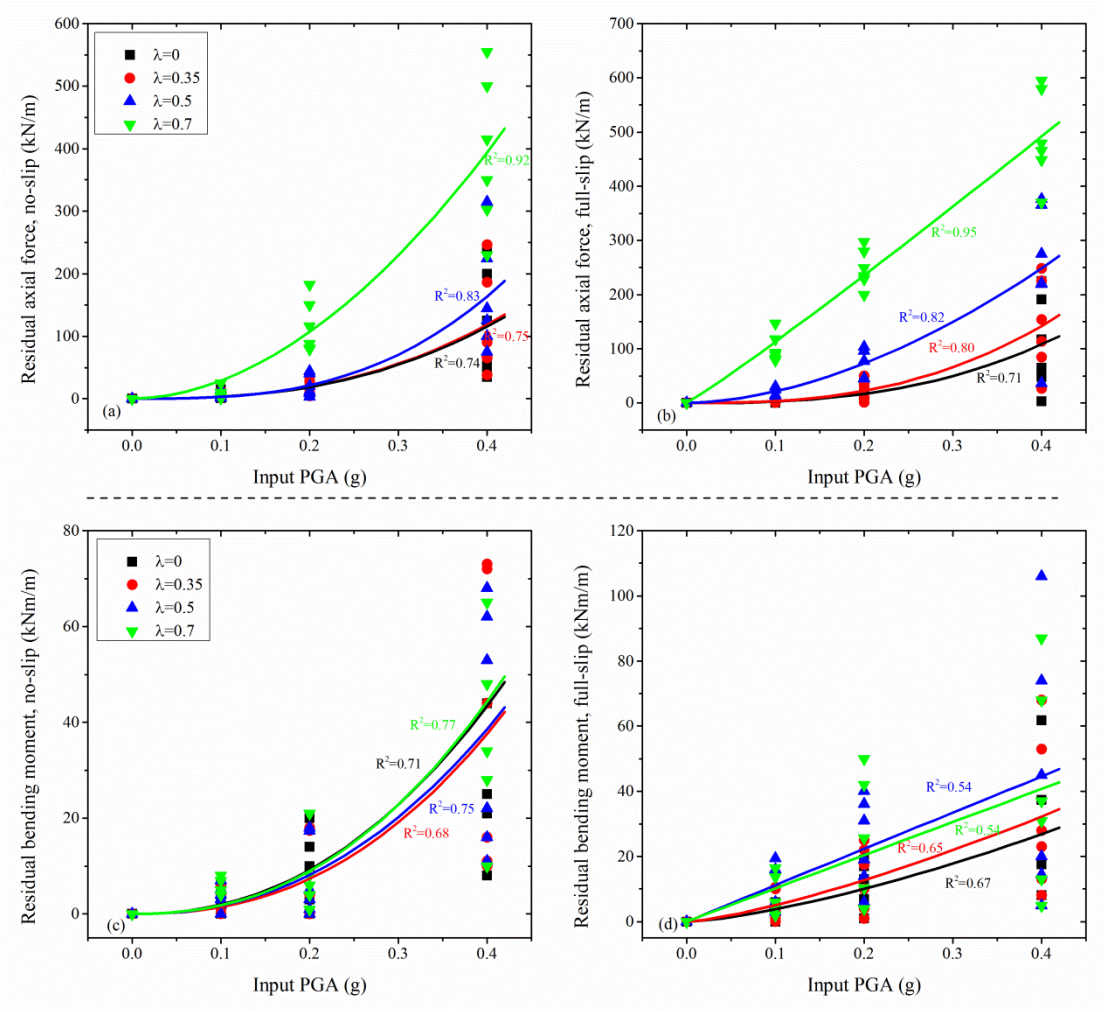

Fig. 19. Relationship between residual internal forces and stress release coefficients: (a) axial forces, no-slip; (b) axial forces, full-slip; (c) bending moments, no-slip; (d) bending moments, full-slip

Fig. 19 summarizes the residual axial forces and residual bending moments at the end of the earthquakes for all examined cases. Note that the stress release coefficients have a more pronounced effect on the residual axial forces rather than the residual bending moments. The residual axial forces increase as the stress release coefficients increase. This is more evident for the larger input motion intensity. However, the residual bending moments seem to be less sensitive to the stress release process, since a weak

relationship between the stress release coefficients and the residual bending moments. An increase in the residual bending moment with increasing input motion intensity is observed for the two interface conditions, as expected. The results indicate that the stress release process could aggravate the residual internal forces to some extent.

5. Discussions

5.1 Surface ground motion

Researches on seismic wave scattering produced by tunnels mainly focus on two aspects. The first set of works concentrates on determining the dynamic behavior of tunnels subjected to seismic waves. The present study belongs to this set. The second set of works focus on the diffracting effects of tunnels on the surface ground motion. To this end, here discusses whether the stress release during tunneling can significantly influence the surface ground motion.

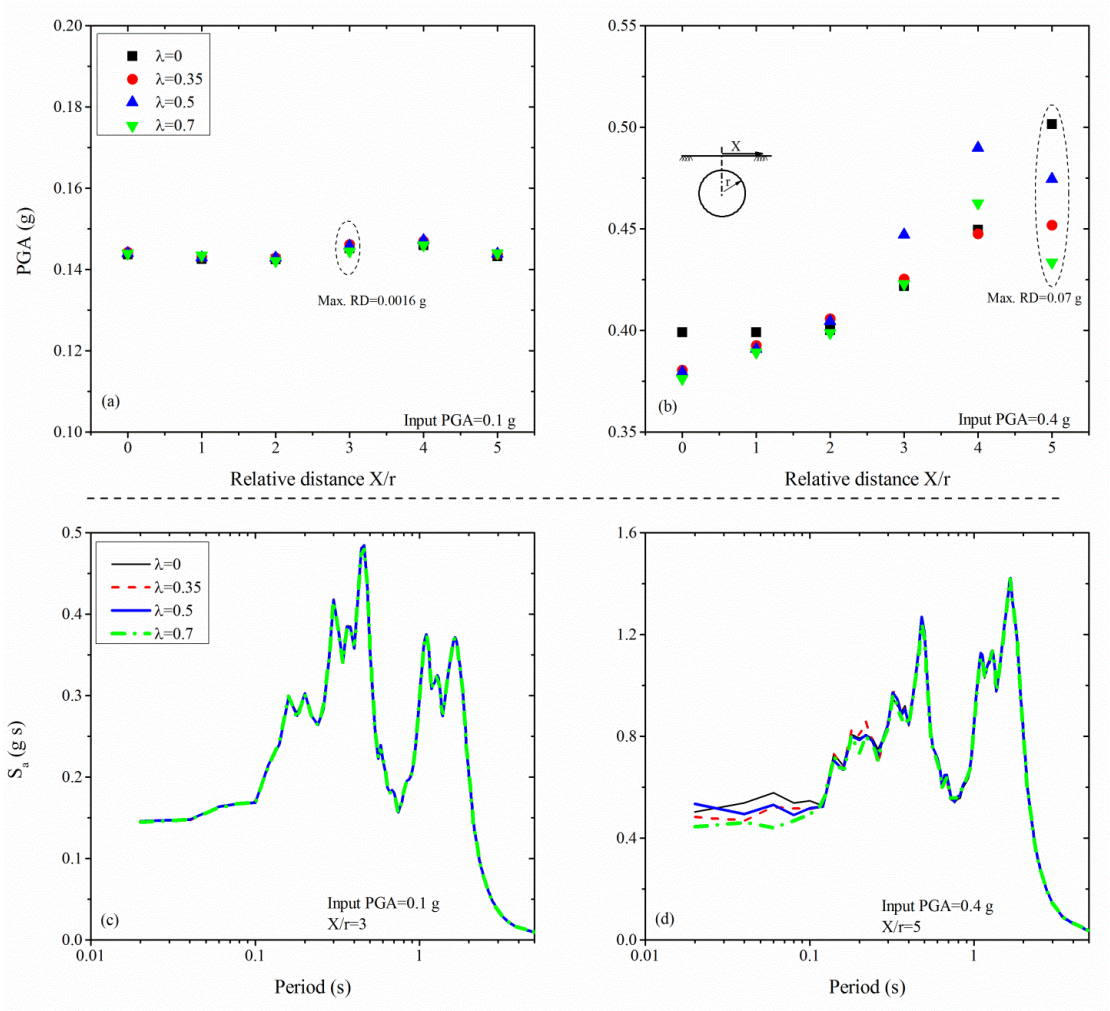

Fig. 20. Acceleration at the ground surface for various stress release coefficients: (a) surface PGA, 0.1 g; (b) surface PGA, 0.4 g; (c) spectral acceleration, 0.1 g; (d) spectral acceleration, 0.4 g (no-slip case, Kobe earthquake)

Fig. 20 shows the peak ground acceleration (PGA) at various relative positions (X/r) and spectral accelerations (S_a) at the ground surface. The relative differences (RD) of surface PGA at various stress release levels are negligible with a maximum RD is equal to 0.0016 g for PGA = 0.1 g while the maximum RD equals to 0.07 g for the 0.4 g case. The surface PGA seems to be strongly related to the relative position (X/r) rather than the stress release coefficient. However, the stress release process has a more pronounced effect on the spectral acceleration for the higher input PGA (Fig. 20d). In general, higher stress release levels result in slightly smaller S_a values over a short period range while no difference is observed over a long period range.

5.2 Minimum damping ratio

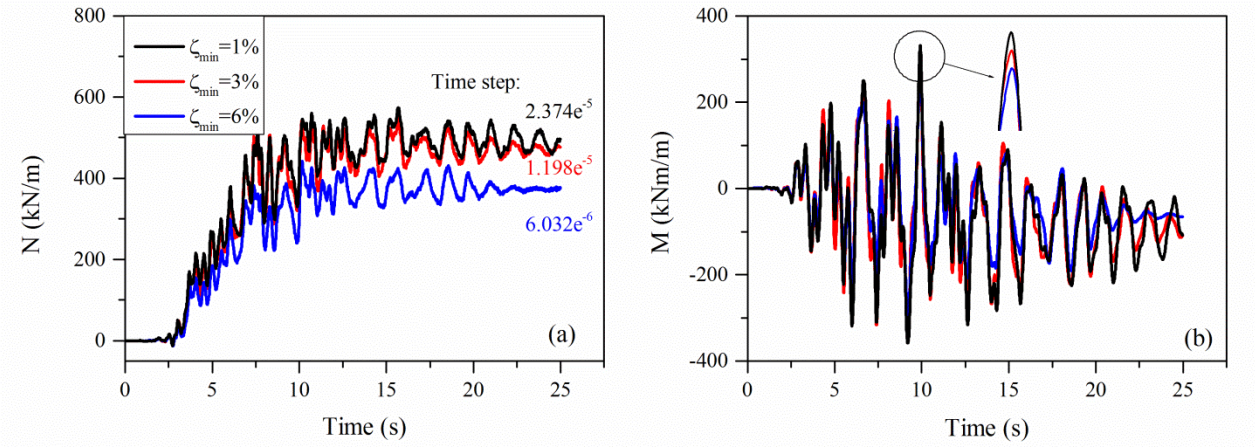

Fig. 21. Time histories of seismic internal forces: (a) axial forces; (b) bending moments

The time histories of the seismic internal force increments for three damping levels (ζ_{min}) are presented in Fig. 21, corresponding to λ= 0.7, subjected to the Kobe earthquake with an amplitude of 0.4 g for the full-slip condition. As can be found, a higher damping ratio reduces the responses in terms of maximum and residual internal forces. In addition, the natural oscillation of the system can be damped out by the higher damping but the calculation time is significantly increased [27]. Table 5 presents the ratios of R_N and R_M. A similar trend between the stress release coefficients and the calculated ratios is captured while larger R_N and R_M ratios are predicted for a smaller damping ratio case. The relative differences of R_N or R_M ratios calculated by various damping ratios generally become larger as the input motion intensities increase, particularly at higher stress release levels. The results illustrate that the selection of an appropriate damping ratio is an important issue in the dynamic time-history numerical analysis, which

needs to be determined with caution [38].

Table 5. R_N and R_M ratios at three damping ratios for the full-slip case

Case		$R_{N\_full-slip}$			$R_{M\_full-slip}$		
		$\zeta_{min} = 1\ \%$	$\zeta_{min} = 3\ \%$	$\zeta_{min} = 6\ \%$	$\zeta_{min} = 1\ \%$	$\zeta_{min} = 3\ \%$	$\zeta_{min} = 6\ \%$
PGA = 0.1 g	λ=0	0.064	0.053	0.045	1.433	1.132	0.885
	λ=0.35	0.069	0.058	0.050	1.602	1.196	0.946
	λ=0.5	0.122	0.069	0.051	2.106	1.507	1.207
	λ=0.7	0.563	0.313	0.209	2.817	2.333	1.853
PGA = 0.2 g	λ=0	0.111	0.080	0.077	2.646	1.927	1.798
	λ=0.35	0.128	0.108	0.083	2.812	1.954	1.876
	λ=0.5	0.298	0.216	0.135	3.459	2.521	2.301
	λ=0.7	1.329	0.757	0.531	5.027	4.044	3.636
PGA = 0.4 g	λ=0	0.497	0.288	0.155	4.37	3.371	2.960
	λ=0.35	0.585	0.336	0.211	4.676	3.696	3.065
	λ=0.5	0.933	0.627	0.402	5.882	5.000	4.268
	λ=0.7	2.038	1.496	1.191	9.333	7.622	6.578

5.3 G/G_{max} curves

The above numerical model adopts a single shear modulus reduction (G/G_{max}) curve. It is a fact that these types of curves for soils are strongly dependent on the mean effective stress. High mean stress results in less damping and modulus reduction. By making the hysteretic damping depth-dependent, the simulation can be more realistic. Hence, the depth-dependent G/G_{max} curves [3] as illustrated in Fig. 4, are used to compare its potential influence on the numerical predictions. Fig. 22 presents the experimental data, the fitted curves and the corresponding values (i.e., L_1 and L_2 in the Eqs. 4 and 5) used in numerical models [20].

Fig. 23 presents the comparison for the full-slip case in terms of the ratios of R_N and R_M. Two scenarios (i.e., single curve and depth-dependent curves) capture similar relations between the R_N (or R_M) ratios with stress release coefficients under different ground motion intensities. The results calculated by the depth-dependent G/G_{max} curves are in well agreement with the ones of the single curve for the smaller stress release coefficients and lower ground motion intensities. The G/G_{max} curve has a more pronounced effect on the axial forces rather than on the bending moments. This effect becomes progressively larger as the stress release coefficients and ground motion intensities increase, reaching respectively differences of 27% and 19.4% for axial forces and bending moments. It can be concluded that the effect of the hysteretic

formulation in the numerical predictions depends on the initial shear stress state and the modulus reduction levels (i.e., ground motion intensities).

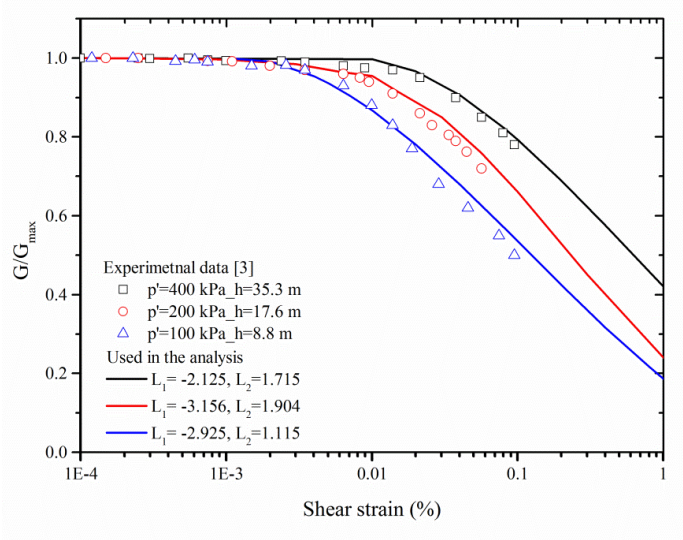

Fig. 22..Depth-dependent G/G_{max} curves [3]

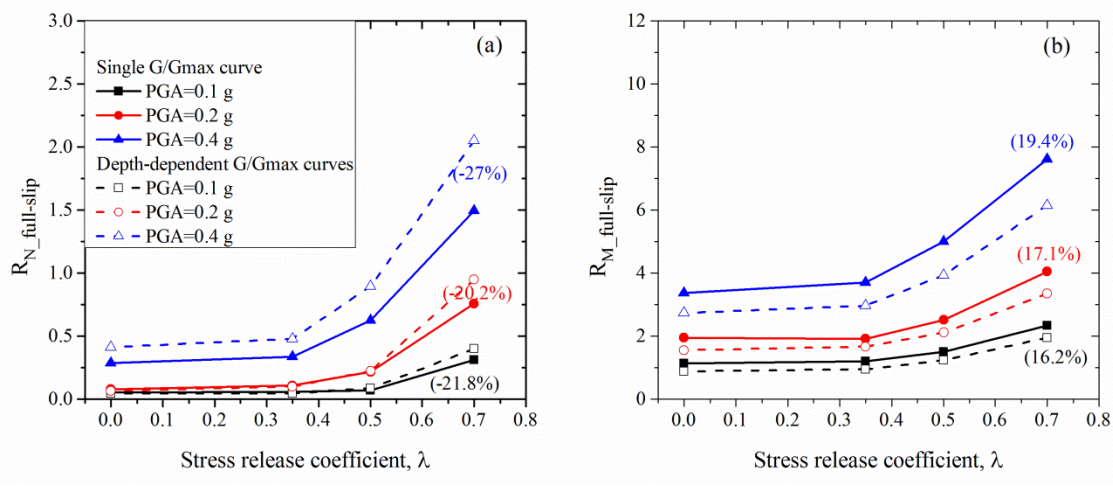

Fig. 23. Time histories of seismic internal forces: (a) axial forces; (b) bending moments

6. Conclusions

A set of two-dimensional dynamic nonlinear time-history analyses combined with the convergence-confinement method were conducted to assess the influence of the stress release process caused by construction on the seismic behavior of tunnels. The numerical model accounted for the frequency characteristics and intensities of the input ground motions at two extreme soil-tunnel interface conditions. The study also discussed the influence of stress release on the surface ground motion and the uncertainties of damping ratio and G/G_{max} curves on the numerical predictions. Based on this parametric

investigation the following conclusions can be drawn:

1. For the static analysis, the lining forces and deformations decreased and the plastic zones became larger as the stress release coefficients increased. Assuming no-slip conditions between the soil and the tunnel led to larger axial forces and lower bending moments.

2. The stress release process produced additional seismic axial force increments whereas the effect was minor for the seismic bending moment increments. Various input ground motions captured similar trends.

3. In terms of R ratios, the stress release process had a more pronounced effect on the bending moment (R_M) rather than the axial force (R_N) with the effect became progressively larger as the stress release coefficient and the input motion intensity increased. In general, the no-slip conditions predicted slightly larger R_N and R_M ratios than the full-slip conditions.

4. With regards to SR ratios, an increase of SR_N ratio with increasing stress release coefficient was found. In general, the stress release process showed a minor influence on SR_M ratios and no clear trend could be observed.

5. The residual axial force in both the no-slip and the full-slip conditions had a tendency of increasing with the stress release coefficients and ground motion levels increased, while the residual bending moment was less sensitive to the stress release coefficients.

6. The stress release process hardly affected the PGA at the ground surface although a large stress release level generally resulted in slightly lower spectral acceleration amplitude over the short period range for high ground motion intensities. A larger damping ratio could reduce the lining forces and time step, thus increased runtimes of dynamic simulations. In addition, the G/G_{max} curves had an important influence on the numerical predictions, particularly for the larger stress release coefficients and higher ground motion intensities.

Appendix

This Appendix summarizes the equations employed by the two analytical solutions for calculating the axial forces and bending moments for the no-slip assumption at the interface in static conditions. The equations are presented using a consistent notation for all solutions, where σ_v and σ_h are respectively vertical and horizontal stresses at the tunnel center depth, r is the tunnel radius, θ is the orientation angle

representing the position of observation points, μ is the soil Poisson's ratio, EI and EA are the flexural rigidity and the normal stiffness of the lining, E_s is the elasticity modulus of the soil.

Bakker method [2]:

$$N = -\frac{(\sigma_v+\sigma_h)}{2}r + \frac{(\sigma_v-\sigma_h)}{2}r\cos(2\theta) \tag{9}$$

$$M = -\frac{(\sigma_v+\sigma_h)}{4}r^2\cos(2\theta) \tag{10}$$

Erdmann method [13]:

The maximum normal force N_{max} and the maximum bending moment M_{max} are respectively given by the following equation:

$$N_{max} = \frac{\alpha\cdot r}{\alpha+\beta+\frac{\alpha\cdot\beta}{1+\mu}}\cdot\frac{(\sigma_v+\sigma_h)}{2} + \frac{(1+\frac{\alpha}{12(1+\mu)}+\frac{\beta}{4(1+\mu)})\cdot r}{1+\frac{\alpha\cdot(3-2\mu)}{12(3-4\mu)(1+\mu)}+\frac{\beta\cdot(5-6\mu)}{4(3-4\mu)(1+\mu)}+\frac{\alpha\cdot\beta}{12(3-4\mu)(1+\mu)^2}}\cdot\frac{(\sigma_v-\sigma_h)}{2} \tag{11}$$

$$M_{max} = \frac{(1+\frac{\beta}{2(1+\mu)})\cdot r^2}{2+\frac{\alpha\cdot(3-2\mu)}{6(3-4\mu)(1+\mu)}+\frac{\beta\cdot(5-6\mu)}{4(3-4\mu)(1+\mu)}+\frac{\alpha\cdot\beta}{6(3-4\mu)(1+\mu)^2}}\cdot\frac{(\sigma_v-\sigma_h)}{2} \tag{12}$$

$$\alpha = \frac{E_s r^3}{EI} \tag{13}$$

$$\beta = \frac{E_s r}{EA} \tag{14}$$

Acknowledgments

The authors gratefully acknowledge the financial support provided by the China Scholarship Council (20170813080).

References

[1] Amorosi A, Boldini D, Falcone G. Numerical prediction of tunnel performance during centrifuge dynamic tests. Acta Geotechnica 2014;9:581-596.

[2] Bakker K. Structural design of linings for bored tunnels in soft ground. Heron 2003;48:33-63.

[3] Bilotta E, Lanzano G, Madabhushi SPG, Silvestri F. A numerical Round Robin on tunnels under seismic actions. Acta Geotechnica 2014;9:563-579.

[4] Cilingir U, Madabhushi SPG. A model study on the effects of input motion on the seismic behavior of tunnels. Soil Dynamics and Earthquake Engineering 2011;31:452-462.

513 [5] Conti R, Viggiani GMB. Numerical modelling of centrifuge dynamic tests of circular tunnels in dry
514 sand. Acta Geotechnica 2014;9:597-612.

515 [6] Corigliano M, Scandella L, Lai CG, Paolucci R. Seismic analysis of deep tunnels in near fault
516 conditions: a case study in Southern Italy. Bulletin of Earthquake Engineering 2011;9:975-995.

517 [7] Croce A. Analisi dati di monitoraggio del rivestimento della galleria del passante ferroviario di Bologna.
518 ([Ph,D. thesis]). Torino: Polytechnics of Torino, 2011.

519 [8] Dias D, Kastner R. Movements caused by the excavation of tunnels using face pressurized
520 shields-analysis of monitoring and numerical modelling results. Engineering Geology
521 2013;152:17-25.

522 [9] Do N.A, Dias D, Oreste P, Djeran-Maigre I. 2D tunnel numerical investigation: the influence of the
523 simplified excavation method on tunnel behaviour. Geotechnical and Geology Engineering
524 2014;32:43-58.

525 [10] Dolezalova M. The influence of construction work sequence on the stability of underground openings.
526 Third International Conference on Numerical Methods in Geomechanics 1979;561-569.

527 [11] Darendeli MB. Development of a new family of normalized modulus reduction and material damping
528 curves. ([Ph,D. thesis]). Austin: University of Texas; 2001.

529 [12] EPRI. Guidelines for determining design basis ground motions. Electric Power Research Institute,
530 Palo Alto, California, Report number: EPRI TR-102293;1993.

531 [13] Erdmann J. Comparison of two-dimensional and development of three-dimensional analysis methods
532 for tunnels. Report Institute of Statics, TU Braunschweig, 83-40, 1983.

533 [14] Gomes RC. Effect of stress disturbance induced by construction on the seismic response of shallow
534 bored tunnels. Computers and Geotechnics 2013;49:338-351.

535 [15] Gomes RC. Numerical simulation of the seismic response of tunnels in sand with an elastoplastic
536 model. Acta Geotechnica 2014;9:613-629.

537 [16] Hashash YMA, Hook JJ, Schmidt B, Yao, JIC. Seismic design and analysis of underground structures.
538 Tunnelling and Underground Space Technology 2011;16:347-293.

539 [17] Hleibieh J, Wegener D, Herle I. Numerical simulation of a tunnel surrounded by sand under
540 earthquake using a hypoplastic model. Acta Geotechnica 2014;9:631-640.

541 [18] Huo HB, Bobet A, Fernandez G, Ramire J. Load transfer mechanisms between underground structure
542 and surrounding ground: evaluation of the failure of the Daikai station. Journal of Geotechnical and
543 Geoenvironmental Engineering 2005;131(12):1522-1533.

544 [19] ITA. Guidelines for the design of tunnels. Tunnelling and Underground Space Technology
545 1988;3:237-249.

546 [20] Itasca. FLAC – Fast Lagrangian Analysis of Continua – Version 7.0 User's Guide. Itasca Consulting
547 Group, Minneapolis; 2011.

548 [21] Karakus M. Appraising the methods accounting for 3D tunnelling effects in 2D plane strain FE
549 analysis. Tunnelling and Underground Space Technology 2007;22:47-56.

550 [22] Karakus M, Fowell RJ. Effects of different tunnel face advance excavation on the settlement by FEM.
551 Tunnelling and Underground Space Technology 2003;18:513-523.

552 [23] Konagai K, Takatsu S, Kanai T, Fujita T, Ikeda T, Johansson J. Kizawa tunnel cracked on 23 October
553 2004 Mid-Niigata earthquake: an example of earthquake-induced damage to tunnels in active-folding
554 zones. Soil Dynamics and Earthquake Engineering 2009;29:394-403.

555 [24] Kontoe S, Zdravkovic L, Potts DM, Menkiti CO. On the relative merits of simple and advanced
556 constitutive models in dynamic analysis of tunnels. Geotechnique 2011;61(10):815-829.

557 [25] Kontoe S, Avgerinos V, Potts DM. Numerical validation of analytical solutions and their use for
558 equivalent-linear seismic analysis of circular tunnels. Soil Dynamics and Earthquake Engineering
559 2014;66:206-219.

560 [26] Kuhlemeyer RL, Lysmer J. Finite element method accuracy for wave propagation problems. Journal
561 of the Soil Mechanics and Foundations Division, ASCE 1973;99 (SM5):421-427.

562 [27] Kwok AOL, Stewart JP, Hashah YMA, Matasovic N, Pyke R, Wang ZL, Yang ZH. Use of exact
563 solutions of wave propagation problems to guide implementation of nonlinear seismic ground
564 response analysis procedures. Journal of Geotechnical and Geoenvironmental Engineering, ASCE
565 2007;133(11):1385-1398.

566 [28] Lanzano G, Bilotta E, Russo G, Silvestri F. Experimental and numerical study on circular tunnels
567 under seismic loading. European Journal of Environmental and Civil Engineering 2015;19:539-563.

568 [29] Lanzano G, Bilotta E, Russo G, Silvestri F, Madabhushi SPG. Centrifuge modeling of seismic loading
569 on tunnels in sand. Geotechnical Testing Journal 2012;35:1-16.

570 [30] Li TB. Damage to mountain tunnels related to the Wenchuan earthquake and some suggestions for
571 aseismic tunnel construction. Bulletin of Engineering Geology and the Environment 2012;71:
572 297-308.

573 [31] Ma C, Lu DC, Du XL, Qi CZ. Effect of buried depth on seismic response of rectangular underground
574 structures considering the influence of ground loss. Soil Dynamics and Earthquake Engineering
575 2018;106:278-297.

576 [32] Manica M, Ovando E, Botero E. Assessment of damping models in FLAC. Computers and
577 Geotechnics 2014;59:12-20.

578 [33] Owen GN, Scholl RE. Earthquake engineering of large underground structures. JAB-7821. San
579 Francisco: URS/John A. Blume ; 1981.

580 [34] Panet M, Guenot A. Analysis of convergence behind the face of a tunnel. Proc Int Symp
581 Tunnelling'82 1982;197-204.

582 [35] Sun JI, Golesorkhi R, Seed HB. Dynamic moduli and damping ratios for cohesive soils. Earthquake
583 Engineering Research Center, University of California, Berkeley, Report No. UCB/EERC-88/15;
584 1988.

585 [36] Sharma S, Judd W R. Underground opening damage from earthquakes. Engineering Geology
586 1991;30:263-276.

587 [37] Sedarat H, Kozak A, Hashash YMA, Shamsabadi A, Krimotat A. Contact interface in seismic analysis
588 of circular tunnels. Tunnelling and Underground Space Technology 2009;24:482-490.

589 [38] Sun QQ, Dias D. Significance of Rayleigh damping in nonlinear numerical seismic analysis of tunnels.
590 Soil Dynamics and Earthquake Engineering 2018;115:489-494.

591 [39] Sun QQ, Dias D. Assessment of stress relief during excavation on the seismic tunnel response by the
592 quasi-static method. Soil Dynamics and Earthquake Engineering 2019;117:384-397.

593 [40] Sun QQ, Dias D, Sousa LR. Impact of an underlying soft soil layer on tunnel lining in seismic
594 conditions. Tunnelling and Underground Space Technology 2019;90:293-308.

595 [41] Tsinidis G, Pitilakis K, Anagnostopoulos C. Circular tunnels in sand: dynamic response and efficiency
596 of seismic analysis methods at extreme lining flexibilities. Bulletin Earthquake Engineering
597 2016;14:2903-2929.

598 [42] Tsinidis G, Pitilakis K. Numerical simulation of round robin numerical test on tunnels using a
599 simplified kinematic hardening model. Acta Geotechnica 2014;9:641-659.

600 [43] Wang WL, Wang TT, Su JJ, Lin CH, Seng CR, Huang TH. Assessment of damage in mountain tunnels
601 due to the Taiwan Chi-Chi Earthquake. Tunnelling and Underground Space Technology
602 2011;16:133-150.

603 [44] Wang ZZ, Zhang Z. Seismic damage classification and risk assessment of mountain tunnels with a
604 validation for the 2008 Wenchuan earthquake. Soil Dynamics and Earthquake Engineering
605 2013;45:45-55.

606 [45] Zhao CY, Lavasan AA, Barciaga T, Kamper C, Mark P, Schanz T. Prediction of tunnel lining forces
607 and deformations using analytical and numerical solutions. Tunnelling and Underground Space
608 Technology 2017;64:164-176.

609 [46] Zhang XP, Jiang YJ, Sugimoto S. Seismic damage assessment of mountain tunnel: a case study on the
610 Tawarayama tunnel due to the 2016 Kumamoto Earthquake. Tunnelling and Underground Space
611 Technology 2018;71:138-148.

612